

Mechanisms of Poleward Propagating, Intraseasonal Convective Anomalies in Cloud System–Resolving Models

WILLIAM R. BOOS

Department of Earth and Planetary Sciences, Harvard University, Cambridge, Massachusetts

ZHIMING KUANG

Department of Earth and Planetary Sciences, and School of Engineering and Applied Sciences, Harvard University, Cambridge, Massachusetts

(Manuscript received 30 March 2010, in final form 1 July 2010)

ABSTRACT

An envelope of convection that propagates both poleward and eastward accounts for the largest fraction of intraseasonal variance of the tropical atmosphere during boreal summer. Here the mechanisms of poleward propagating convective anomalies are examined in a nonhydrostatic model with zonally symmetric boundary conditions, integrated on a beta plane at resolutions high enough to explicitly represent moist convection. When the domain has a narrow zonal dimension of 100 km or less, the model produces a quasisteady intertropical convergence zone (ITCZ). Meridionally propagating transients are produced for some prescribed sea surface temperature distributions, but these transients are shallow, vanish at finer resolutions, and have a structure that bears little resemblance to that of observed poleward propagating anomalies. This is in sharp contrast to previous studies that obtained robust poleward propagating anomalies in axisymmetric models using parameterized moist convection, and it suggests that the anomalies seen in those models may be caused by deficient representations of dynamics or subgrid-scale physics.

Robust poleward propagating anomalies are obtained when the high-resolution, nonhydrostatic model is integrated in a wider domain with a zonal dimension near 1000 km. Diagnostics suggest that poleward propagation in this wide domain results from the convectively coupled beta drift of low-level vorticity anomalies. Deep near-equatorial ascent produces low-level cyclones that migrate poleward through the process of beta drift; Ekman pumping in these drifting cyclones then humidifies the free troposphere ahead of the initial deep ascent, shifting the convection poleward. The moist static energy budget and model sensitivity tests suggest that these anomalies can be viewed as moisture modes destabilized through a moisture–radiation feedback. Wind–evaporation feedback also seems to contribute to the instability of these anomalies, but because it enhances surface fluxes on the equatorward side of the anomalies, it also reduces their propagation speed. These results suggest a novel mechanism for the poleward propagation of intraseasonal convective anomalies and illustrate the need to evaluate theoretical models that use parameterized convection against cloud system–resolving models.

1. Introduction

During boreal summer, an envelope of deep convection that moves both poleward and eastward accounts for the largest fraction of intraseasonal (10–90 day) variance of the tropical atmosphere; this is often referred to as the intraseasonal oscillation (ISO). The eastward propagating component is widely known as the Madden–Julian

oscillation (MJO) and is also observed during all other seasons (Madden and Julian 1972). The poleward propagating component has been documented only during boreal summer; while it is traditionally associated with episodic variations in the intensity of the South Asian summer monsoon (Yasunari 1979; Goswami 2005), similar behavior has been documented in the tropical east Pacific (Maloney et al. 2008; Jiang and Waliser 2008). While the eastward propagation typically occurs at a speed near 5 m s^{-1} , poleward speeds range from 1 to 2 m s^{-1} , with speeds in the faster part of that range typically occurring in Asian longitudes (Goswami 2005; Jiang and Waliser 2008).

Corresponding author address: William R. Boos, Department of Geology & Geophysics, Yale University, P.O. Box 208109, New Haven, CT 06520-8109.
E-mail: billboos@alum.mit.edu

a. Phenomenology

In both Asian longitudes and the eastern Pacific, composites of the boreal summer ISO reveal a zonally elongated, northwest–southeast-tilted band of convection that forms over the near-equatorial ocean and migrates northward and eastward (Wheeler and Hendon 2004; Goswami 2005; Webster 2006; Jiang and Waliser 2008). It has been suggested that this structure results from the continual emanation of Rossby waves by eastward-moving convection associated with the MJO, producing a sort of northwest–southeast-tilted convective front (Wang and Xie 1997). However, Wang and Rui (1990) found that only about half of the poleward propagating ISO events in Asia occurred concurrently with eastward propagation. While Lawrence and Webster (2002) estimated this fraction to be higher, use of a more inclusive criterion for ISO activity does seem to produce a fraction closer to 50% (Jones et al. 2004; Goswami 2005). Furthermore, many general circulation models (GCMs) poorly represent the eastward propagating MJO but do simulate at least some form of poleward propagating, intraseasonal convective anomaly during boreal summer (Lin et al. 2008), suggesting that the two phenomena may result from different mechanisms. Note that this manuscript is concerned with the 30–60-day ISO and does not address the physics of the 10–20-day mode associated with the westward propagation of convective anomalies from the equatorial western Pacific (Krishnamurti and Bhalme 1976; Annamalai and Slingo 2001).

In the east Pacific, the intraseasonal northward propagation of convection is confined to oceanic regions near the intertropical convergence zone (ITCZ; Jiang and Waliser 2008). In Asian longitudes, the convective anomalies migrate from the near-equatorial Indian Ocean to the South Asian landmass where they modulate the intensity of monsoonal precipitation. Convection in Asia spends more time near the equator and the poleward limit of its excursions than in intermediate latitudes, however, resulting in time-mean low-level convergence zones near the equator and 20°N in summer climatologies (Sikka and Gadgil 1980). And even in Asia, the highest intraseasonal variance is located over ocean, with the intraseasonal variance that does occur over land largely confined to the peninsular regions of India and Indochina; it has been argued that this is consistent with wind-induced surface heat exchange (WISHE) being central to the physics of the ISO (Sobel et al. 2008). ISO activity has been shown to be anticorrelated with monsoon intensity, with low summer mean precipitation occurring over India when ISO variance is high, in a manner seemingly uncorrelated with the El Niño–Southern Oscillation (Lawrence and Webster 2001). This

relationship has led to the suggestion that changes in mean monsoon intensity result primarily from changes in the characteristics of the ISO (Palmer 1994).

The poleward propagating ISO exhibits a distinct vertical and meridional structure, with positive low-level anomalies of convergence and humidity lying north of maxima in deep convection and precipitation (Kemball-Cook and Wang 2001; Jiang et al. 2004). Both humidity and vertical velocity exhibit a southward tilt with height through the depth of the troposphere, although some reanalysis datasets do not show this tilt as clearly as others in the humidity field (Jiang et al. 2004; Jiang and Waliser 2008). A free-tropospheric vorticity maximum also lies slightly north of the convection; although some authors call this a barotropic vorticity anomaly (Jiang et al. 2004; Bellon and Sobel 2008a), it has a clear midtropospheric maximum and decays strongly with height between 400 hPa and the tropopause, so it is unclear whether it projects more strongly onto a barotropic or some higher baroclinic mode.

b. Theory

We noted above that up to half of northward propagating ISO events in Asia seem to occur without concurrent eastward propagation and that some GCMs simulate northward propagation without successfully representing the eastward propagating MJO. It is thus not surprising that theoretical studies have posited separate mechanisms for the eastward and poleward propagating components of the ISO. Some studies have used axisymmetric (latitude–height) models in attempts to understand the mechanism responsible for poleward migrations, and such models, by construction, cannot represent zonally propagating phenomena. Based on an axisymmetric model of a monsoon climate with an off-equatorial land surface, Webster and Chou (1980) argued that land surface hydrology was essential to the poleward propagating ISO [see also Webster (1983)]. This mechanism was generalized in a later study to show that a poleward gradient of convective instability could produce poleward propagation of convective anomalies over ocean (Srinivasan et al. 1993). As in all models of the phenomenon constructed to date, these studies employed parameterized convection, and the characteristics and very existence of poleward propagating anomalies in these models may be highly dependent on the nature of the convective closure.

Several recent studies, also employing parameterized convection, have shown how poleward propagation of deep convection might be generated by momentum exchange between dynamical anomalies and the baroclinic summer mean state. Jiang et al. (2004) found that anomalous vertical advection of mean zonal momentum could

produce anomalous barotropic vorticity poleward of an initial ascent anomaly, through tilting of the mean state horizontal vorticity [see also Drbohlav and Wang (2005), (2007)]. Ekman pumping caused by the free-tropospheric barotropic vorticity anomaly was invoked to produce low-level ascent and convection poleward of the original ascent anomaly, thereby shifting convection poleward. In a different axisymmetric model, Bellon and Sobel (2008a) found that advection of baroclinic vorticity anomalies by the mean baroclinic meridional wind projects strongly onto a barotropic mode, producing barotropic vorticity poleward of an ascent anomaly. They also proposed that Ekman pumping by this induced barotropic vorticity anomaly would shift convection poleward [see also Bellon and Sobel (2008b)].

Although the mechanisms proposed by Jiang et al. (2004) and Bellon and Sobel (2008a) rely on momentum exchange between anomalies and the vertically sheared mean flow to produce poleward propagation, they produce instability only with the addition of parameterized moist convection, and understanding the interaction of this convection with dynamics is difficult, even in idealized models. Jiang et al. (2004) did not explicitly define an instability mechanism that maintained their anomalies against dissipation, although they employed a moisture-convergence closure that might produce conditional instability of the second kind (CISK; e.g., Arakawa 2004). They also found that meridional moisture advection and air-sea interaction were important near the equator in their model. Bellon and Sobel (2008b) found that WISHE was needed to destabilize anomalies in their model, although they noted that instability could be obtained without WISHE for certain parameters; what causes this instability in the absence of WISHE was unclear.

All of the studies discussed above used parameterized convection to explore their proposed mechanisms, and the growth rates and phase speeds of anomalies predicted by these studies have been shown to depend on the details of those parameterizations (e.g., Bellon and Sobel 2008b). The main goal of this paper is to determine whether poleward propagating convective anomalies are produced in a nonhydrostatic model integrated at resolutions high enough to explicitly represent deep moist convection, thereby eliminating dependence on a particular convective closure. As is discussed below, this cloud system-resolving model (CSRM) failed to produce robust poleward propagating deep convective anomalies when integrated in domains without large-scale zonal asymmetries. This suggests that all previous theories based on axisymmetric models may contain deficiencies in their dynamics or subgrid-scale physics. It will be shown below that our CSRM does produce

poleward propagating deep convective anomalies when integrated in a domain wide enough to permit large-scale zonal asymmetries. This result will be used to suggest a new mechanism for poleward propagation of the ISO.

The next section of this paper describes the CSMR and its configuration. Subsequent sections first present results for narrow, nearly axisymmetric domains and then for domains wide enough to represent zonally asymmetric large-scale eddies over a limited range of wavelengths. The last parts of the paper examine the mechanisms for propagation and instability in the wide-domain CSMR and discuss implications and relevance to observations.

2. Model description

We use the System for Atmospheric Modeling (SAM) version 6.3, which is based on the anelastic equations of motion with prognostic equations for liquid water moist static energy, total precipitating water, and total non-precipitating water (Khairotdinov and Randall 2003). This model employs a five-class bulk microphysics scheme, with cloud water, cloud ice, rain, snow, and graupel. Some configuration details are discussed here, but the reader is directed to Khairotdinov and Randall (2003) for a full description of the model.

The model was integrated in a meridional “bowling alley” configuration on an equatorial beta plane extending from 70°N to 70°S. The model was periodic in the zonal direction, and the zonal dimension had at least four grid points in all runs to allow convection to be at least somewhat three-dimensional. Although the narrowest domains are thus not strictly axisymmetric, they are sufficiently narrow that no large-scale eddy activity occurs. A range of horizontal resolutions and zonal widths was employed, described in subsequent sections. All integrations used 48 vertical levels, with vertical grid spacing ranging from 140 m near the surface to 1.6 km near the rigid lid at 48 km. Sponge layer damping in the upper third of the domain was imposed to reduce gravity wave reflection and resonance. We employed a simple Smagorinsky-type closure for the effects of subgrid-scale turbulence. Runs employed default time steps ranging from 6 to 72 s, depending on model resolution; SAM uses second-order Adams–Bashforth time stepping with a variable time step that is halved when the Courant number is high.

A zonally symmetric distribution of sea surface temperature (SST) was prescribed, with an off-equatorial maximum chosen to produce a mean off-equatorial location of the ITCZ, qualitatively similar to that seen in South Asia and the eastern Pacific during boreal summer. Most runs were integrated using SSTs having the same meridional distribution as the thermal forcing chosen

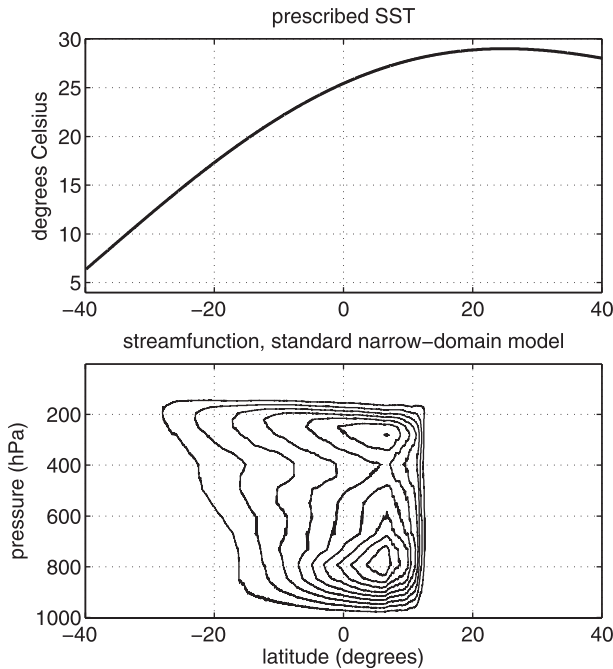


FIG. 1. (top) SST forcing and (bottom) time-mean mass streamfunction for the narrow-domain model at 1-km horizontal resolution. Streamfunction contours show counterclockwise rotation with a contour interval of $5 \times 10^8 \text{ kg s}^{-1}$.

by Lindzen and Hou (1988) in their idealized study of solstitial Hadley circulations:

$$\text{SST}_{\text{LH}} = T_0 - \Delta T (\sin\phi - \sin\phi_0)^2, \quad (1)$$

with $T_0 = 302 \text{ K}$, $\Delta T = 20 \text{ K}$, and $\phi_0 = 25^\circ\text{N}$. This distribution is illustrated in Fig. 1a. Note that although this distribution has quantitative differences with observed SST in both Asian longitudes and the east Pacific, it was chosen both for conceptual simplicity and to produce a mean state qualitatively similar to that produced by the combined thermal forcing of both ocean and land surfaces during northern summer. To assess sensitivity to SST, many integrations were repeated using $\Delta T = 10 \text{ K}$, and some were repeated using the SST employed by Bellon and Sobel (2008a) in their study of poleward propagating convective anomalies. Although ocean coupling is not represented in our models, one might expect it to reduce the influence of WISHE because the ocean would no longer provide an infinite reservoir of energy. Since turning off WISHE altogether will be shown to increase the speed of poleward propagation in our wide-domain model, one might expect ocean coupling to simply enhance propagation speed in that model.

Surface fluxes of momentum, sensible heat, and moisture were calculated using a bulk surface formula where

the wind speed $|\mathbf{V}|$ incorporated a prescribed subgrid-scale gustiness v_g of 1 m s^{-1} :

$$|\mathbf{V}| = \sqrt{u^2 + v^2 + v_g^2}. \quad (2)$$

Here u and v denote the zonal and meridional wind at the lowest model level. Parameterizations from the National Center for Atmospheric Research (NCAR) Community Climate Model (CCM), version 3.5, were used for longwave and shortwave radiation (Kiehl et al. 1998). Radiative fluxes were calculated every 5 min, and diurnal mean insolation for the equinox was prescribed for simplicity.

Some runs were integrated in domains having a larger zonal width of 960 km, and the Reduced Acceleration in the Vertical (RAVE) rescaling of Kuang et al. (2005) was used to reduce the computational burden of these runs. This method reduces the scale separation between convective and large-scale circulations, allowing the interaction between nonhydrostatic convective motions and large-scale flow to be modeled at coarser resolutions without convective parameterization. Integrations conducted with the RAVE rescaling used a horizontal resolution of 30 km and a RAVE factor of 15; results were found to be very similar for RAVE factors as low as unity, which amounts to turning off the rescaling. Thus, while the RAVE method does result in an effective slowing of convection (Pauluis et al. 2006), this slowing seems to have little effect on the poleward propagating convective anomalies that are the focus of this study. Furthermore, we have found that in simulations using the Weather Research and Forecasting (WRF) model, a horizontal grid size of 40–80 km with a RAVE factor of 10–20 can produce reasonable tropical spectra and a poleward propagating ISO without any cumulus parameterization. Strong convectively coupled waves were also seen in equatorial beta-plane simulations run at 40 km resolution with a RAVE factor of 10 (Kuang et al. 2005).

3. Narrow-domain results

For comparison with studies that used axisymmetric models with parameterized convection, we first examined whether poleward propagating convective anomalies were produced in a CSRM integrated in domains sufficiently narrow so as to have no large-scale zonal asymmetries. One integration was conducted at 1-km horizontal resolution and another at 4-km horizontal resolution, both with four grid points in the zonal dimension. As stated in the previous section, all integrations were conducted on a beta plane extending from 70°N to 70°S . While this configuration is not strictly axisymmetric,

any zonally asymmetric eddies will have zonal scales less than 16 km and might be viewed as three-dimensional convective motions rather than large-scale flow.

As expected, when forced by the SST distribution (1) with $\Delta T = 20$ K, the time-mean circulation for both resolutions consisted of a cross-equatorial Hadley circulation, with a narrow region of ascent on the warm side of the equator and a broad region of subsidence on the cold side (Fig. 1b shows the meridional mass streamfunction for the run with 1-km resolution). The ITCZ is located near 10°N , well south of the peak SST but qualitatively consistent with previous studies of the dry dynamics of axisymmetric Hadley circulations (Lindzen and Hou 1988). Northward flow is concentrated in the lowest 200 hPa of the atmosphere. The circulation has a two-celled structure in the vertical, with one cell centered near 800 hPa and another near 300 hPa, qualitatively similar to that seen in other simulations of moist, idealized Hadley circulations centered on the equator (e.g., Nolan et al. 2007). We refrain from examination of the dynamics responsible for the structure of this mean state for purposes of brevity, as there are numerous theories for how the position of the time-mean ITCZ is set by the SST [see review by Sobel (2007)], and for the vertical structure of cross-equatorial circulations (Bretherton et al. 2005; Nolan et al. 2007; Toma and Webster 2010). However, we do note that the mean ITCZ is located just several degrees poleward of the latitude of largest SST curvature (6°N), which would set the location of peak convection in the theory of Lindzen and Nigam (1987).

The ITCZ did exhibit some variability in its position in the run with 1-km horizontal resolution, wandering irregularly between 8° and 14°N , but it showed no regular poleward propagation (Fig. 2a). Considerable transient activity existed both in the winter midlatitudes (not shown) and poleward of the mean ITCZ in the summer hemisphere, but this did not seem directly relevant to the tropical ISO and so is not examined here.

The circulation in these narrow domains was sensitive to horizontal resolution in that northward propagating convective anomalies were produced for 4-km and coarser horizontal resolutions, but not for the finer resolution of 1 km (Fig. 2b). In the run with 4-km resolution, periodic northward propagating anomalies formed after about 100 days of model time. Unlike the repeated northward migration of the main ITCZ seen in the models used by Webster (1983), Jiang et al. (2004), and Bellon and Sobel (2008a), the main ITCZ in this model remained nearly stationary at about 18°N and the propagating anomalies repeatedly merged into it.

The structure of the northward propagating anomalies can be seen in zonal-mean composites produced by

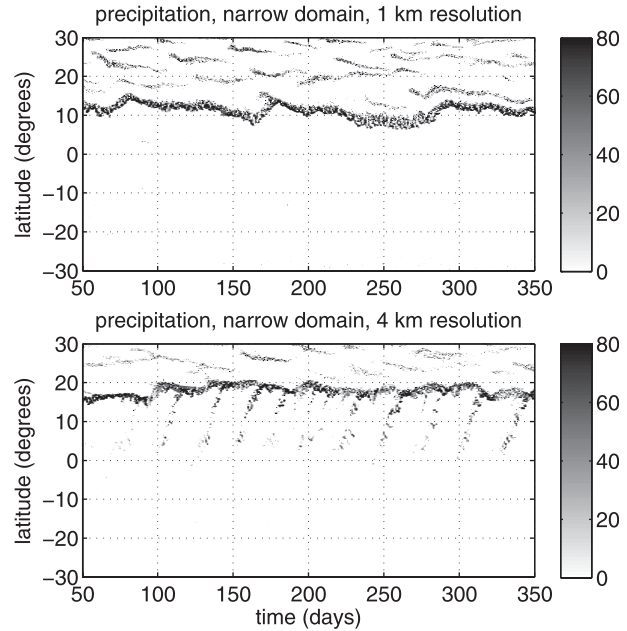


FIG. 2. Time series of precipitation (mm day^{-1}) for the narrow-domain model using the SST shown in Fig. 1. Horizontal resolution is (top) 1 and (bottom) 4 km.

averaging over times when the peak anomalous precipitation was centered at 10°N . The composites were based on the 10 strongest events between days 100 and 350 of the run with 4-km resolution, with anomalies obtained by subtracting the time mean over the same period. These composites show that the anomalies are qualitatively different in many respects from both the observed poleward propagating ISO and the poleward propagating events obtained in previous idealized models. First, the anomalies obtained in this narrow-domain model seemed to originate south of the equator, as evidenced by the surface meridional wind field, although the anomalies had a higher frequency in the Southern Hemisphere with only every second or third event amplifying as it approached the equator (Fig. 3).

Also, the model anomalies are relatively shallow, with almost all outflow confined below 400 hPa (Fig. 4). There is a coherent zonal wind anomaly, but it projects strongly onto modes other than just the barotropic and first baroclinic, and the westerly anomaly has little, if any, statistically significant surface signal. Anomalous ascent peaks near 800 hPa and is almost entirely confined to altitudes below the 500-hPa surface (Fig. 5). These structural properties are quite different from those of the observed poleward propagating ISO, which has a deep baroclinic structure with peak outflow in the upper troposphere near 150 hPa, a strong surface zonal wind signal, and a vorticity anomaly centered slightly north of the peak

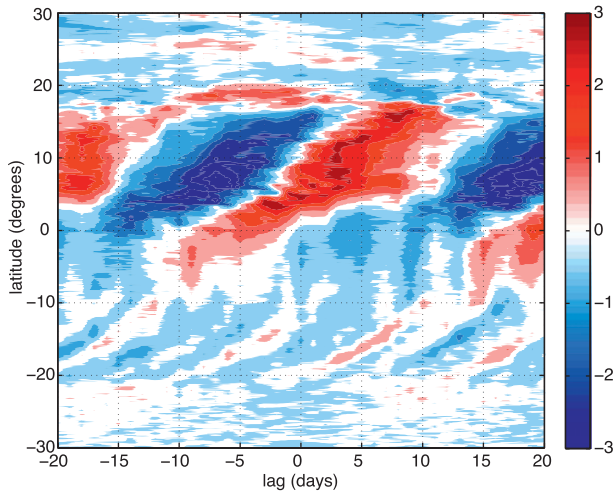


FIG. 3. Composite time series of surface meridional wind (m s^{-1}) for the narrow-domain model at 4-km horizontal resolution, using the SST shown in Fig. 1. Events were selected for the composite based on precipitation at 10°N at lag 0. Red shading denotes northward flow.

precipitation and extending from the surface to about 200 hPa (Jiang et al. 2004).

These shallow, northward propagating anomalies are sensitive to SST as well as resolution, almost vanishing when the SST gradient was reduced by using $\Delta T = 10 \text{ K}$ in (1) at 4-km horizontal resolution (Fig. 6a). Also, when forced by the same SST that produced robust poleward propagating anomalies in the model of Bellon and Sobel (2008a), our narrow-domain model at 4-km resolution produced a nearly steady ITCZ just north of the equator (Fig. 6b). Meridional propagation of convective anomalies toward the main ITCZ was occasionally seen for both of these SST distributions, but such behavior was infrequent and irregular. However, it is worth noting that propagation of shallow convective anomalies in the narrow-domain model was always toward a main ITCZ, and that the propagation speed generally increased with the intensity of the mean Hadley circulation. This would be consistent with the meridional propagation being due to some interaction with the mean baroclinic flow, along similar lines to the mechanisms proposed by Jiang et al. (2004) and Bellon and Sobel (2008b), but with the anomalies failing to deepen and develop a strong surface wind signal. It would also be consistent with the propagation being due simply to the advection of moisture anomalies by the mean low-level flow.

Additional narrow-domain model runs also failed to produce deep, poleward propagating convective events. The SST distributions shown in Fig. 6 were used as a lower boundary condition for the narrow-domain model at 1-km resolution and resulted in behavior similar to

that obtained at 4-km resolution. We also integrated the model with several alternate SST distributions, but any migrating convective disturbances had a shallow structure and characteristics similar to those obtained for $\Delta T = 20 \text{ K}$. Similar results were obtained when the number of zonal grid points was increased from 4 to 12 at the resolution of 4 km, which suggests that the absence of deep, poleward propagating anomalies is not due to moist convection being constrained to be overly two-dimensional by the narrow domain.

In summary, the narrow-domain model failed to produce deep, poleward propagating convective anomalies similar to observations, despite our use of multiple horizontal resolutions, domain widths, and SST distributions. Shallow anomalies that propagate toward a quasi-steady ITCZ were produced for certain particular combinations of horizontal resolution and SST, but these anomalies had characteristics quite different from those of the observed poleward propagating ISO. Understanding the mechanism that produces these shallow anomalies is left for future work, as it is unclear whether they have any relevance to the observed tropical atmosphere.

4. Wide-domain results

To examine whether large-scale, zonally asymmetric eddies might alter the results, we conducted integrations with a domain width of 960 km. Such integrations would be prohibitively expensive at a horizontal resolution of 1 km, so we employed the RAVE rescaling discussed in section 2, with a horizontal resolution of 30 km and a RAVE factor of 15. While this domain width is too narrow to represent baroclinic midlatitude eddies or the Rossby gyres of the MJO, it can accommodate some of the transient eddies often associated with the ITCZ (e.g., Nieto Ferreira and Schubert 1997). Axisymmetric models used in previous studies have assumed that these ITCZ eddies act diffusively (e.g., Sobel and Neelin 2006); we argue below that they may play a dynamically active role in the boreal summer ISO.

When forced with the SST distribution given by (1) with $\Delta T = 20 \text{ K}$, this model produced regular, high-amplitude, poleward propagating convective anomalies (Fig. 7a). In a typical event, the ITCZ would form just north of the equator, persist near 5°N for tens of days, and then migrate northward to about 25°N at a speed near 0.5 m s^{-1} . Poleward propagation always continued to 30°N or more, past the SST maximum, but at a slower speed at latitudes north of about 23°N . Similar behavior was obtained when the SST gradient was reduced by setting ΔT to 10 K, and the results were almost entirely insensitive to variations in the RAVE factor from 1 to 15. No difference in propagation speed could be discerned

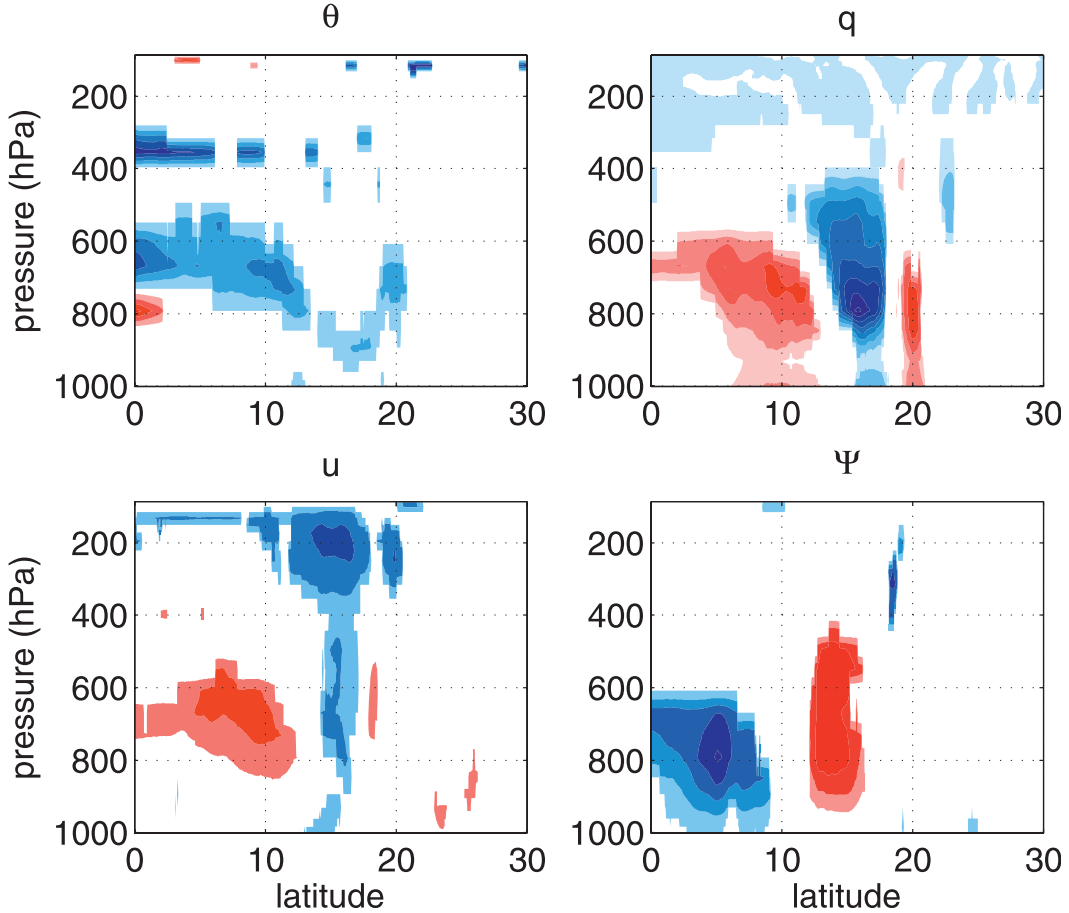


FIG. 4. Composite anomalous structure of poleward propagating convective events in the narrow-domain model at 4-km horizontal resolution: (top left) potential temperature with a contour interval of 0.5 K , (top right) specific humidity with a contour interval of 0.5 g kg^{-1} , (bottom left) zonal wind with a contour interval of 2 m s^{-1} , and (bottom right) mass streamfunction with a contour interval of $5 \times 10^8\text{ kg s}^{-1}$. Only anomalies significant at the 95% level are shown. Red (blue) shading denotes positive (negative) anomalies.

between the runs using $\Delta T = 10\text{ K}$ and $\Delta T = 20\text{ K}$ (not shown); the vertical shear of zonal wind at 15°N varied by a factor of 2 between these runs, which shows that the propagation speed is insensitive to vertical shear, contrary to the mechanism of Jiang et al. (2004).

We conducted one integration at the higher horizontal resolution of 4 km with no RAVE rescaling but with the same domain size (70°N – 70°S , 960-km zonal width). Because of the high computational cost, we could not conduct sensitivity experiments at this resolution similar to those presented in the next section for the 30 km run with RAVE rescaling. Tropical variability in this integration was less regular than for the runs that employed a horizontal resolution of 30 km, and the initial spinup time was longer, but the model did produce deep, poleward propagating convective anomalies with phase speeds similar to those seen in the runs using 30-km resolution (Fig. 7b). Even the reduction in poleward propagation

speed in the northern part of the trajectory was similar, although this reduction occurred about 5° latitude farther south in the run without RAVE. The vertical structure of the wind and thermodynamic fields was highly similar to that seen in the 30-km runs (not shown). Unfortunately, it was not computationally feasible to reduce the grid spacing of the wide-domain model to 1 km; although intraseasonal variability in the narrow domain exhibited a qualitative change in behavior when going from 4-km to 1-km horizontal resolution, a similar change cannot necessarily be expected to occur in the wide domain because the wide-domain behavior seemed much more robust to changes in SST and resolution.

As was done for the narrow-domain model, the zonal-mean structure of poleward propagating events was diagnosed by forming composites based on precipitation. However, composites for the wide-domain model were based on the precipitation at 15°N because 10°N —the

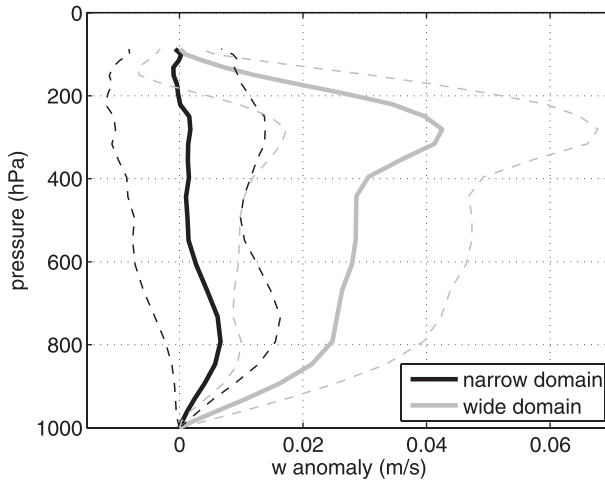


FIG. 5. Composite anomalous vertical velocity for the narrow-domain model at 4-km horizontal resolution in the range 7.0° – 13.0° N (black lines) and for the wide-domain model at 30-km resolution in the range 12.0° – 18.0° N (gray lines). Solid lines denote the composite mean; dashed lines denote a 95% confidence interval based on Student's *t* test.

latitude used for composites in the narrow-domain model—was too close to the somewhat irregular initiation point of the events. Also, composites of total fields, rather than anomalies, were plotted because the mechanism we propose below for the propagation of convective events in this model relies on the nonlinear

evolution of the total wind field, rather than the interaction of an anomaly with a background or mean state. This is not to say that the mean state is irrelevant to the dynamics, but simply that our proposed mechanism is best explained using total fields. A time- and meridional-mean vertical structure was subtracted from the temperature and humidity fields to aid in distinguishing horizontal variations from strong vertical gradients in these quantities.

The resulting composites show several strong similarities to the observed poleward propagating ISO. A cyclonic anomaly has a strong surface signal and a southward tilt with height (Fig. 8). Ascent is deep, with outflow just below the tropopause, and is much stronger than in the narrow-domain model (Fig. 5). Although it is difficult to see in the plots presented here, the lowest part of the cyclonic zonal wind anomaly is centered slightly north of the deep ascent. All of these characteristics are consistent with composites of the ISO based on reanalysis data (Jiang et al. 2004). At 15° N, the latitude of the precipitation maximum in these composites, the temperature field in the wide-domain model consists roughly of a cold over a warm anomaly, which is different from the warm over cold anomaly seen in the reanalysis composites. A humidity anomaly is centered near 700 hPa at an altitude higher than in the reanalysis but similar to that seen in satellite data (Fu et al. 2006).

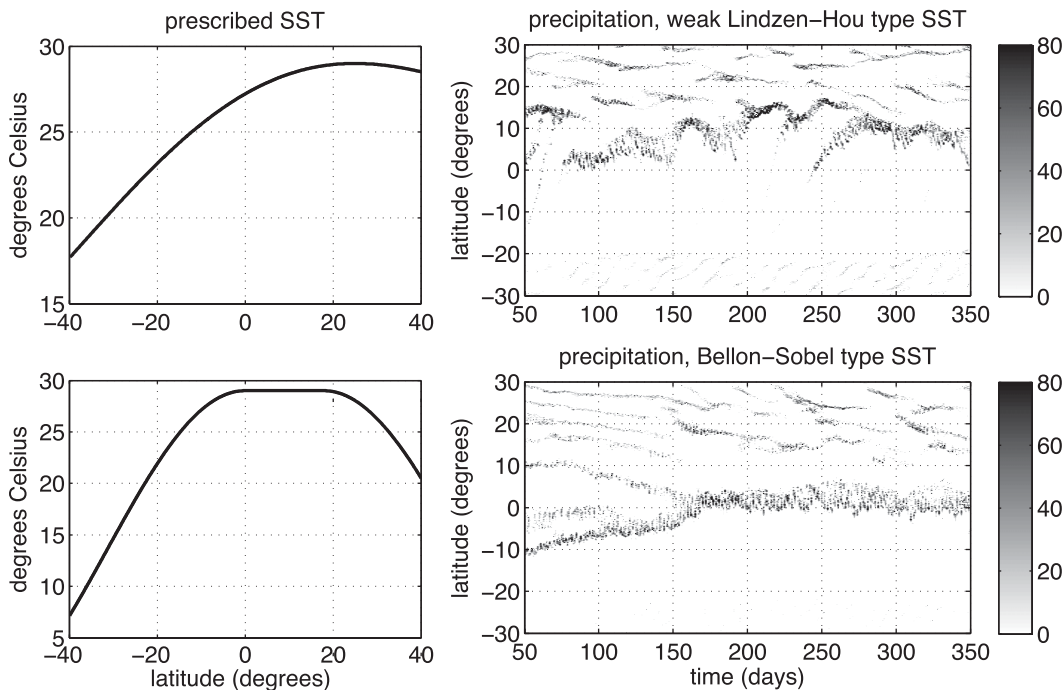


FIG. 6. (left) Prescribed SST and (right) time series of precipitation (mm day^{-1}) for the narrow-domain model at 4-km horizontal resolution. (top) SST given by (1) with $\Delta T = 10$ K; (bottom) SST used by Bellon and Sobel (2008a).

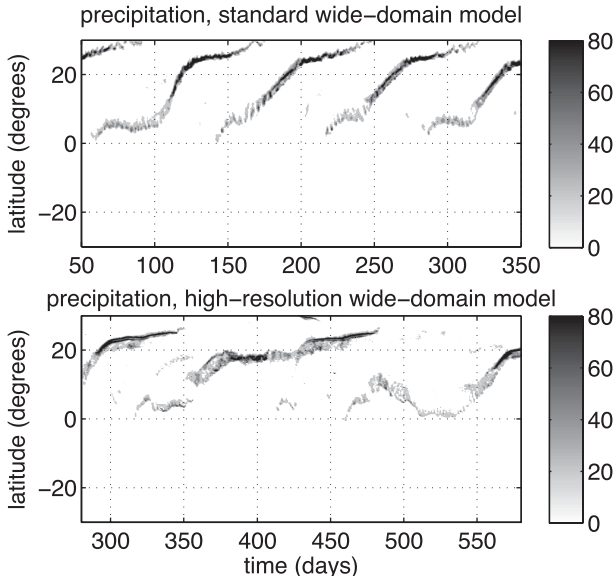


FIG. 7. Time series of precipitation (mm day^{-1}) for the wide-domain model at (top) 30-km horizontal resolution with RAVE factor 15 and (bottom) 4-km horizontal resolution with no RAVE rescaling.

The strong low-level vorticity signal centered at the leading edge of the ascent suggests a possible mechanism for these poleward propagating events in the wide-domain model. This relative vorticity maximum is much larger than the planetary vorticity, producing a strong local maximum in the zonal-mean low-level absolute vorticity (Fig. 9) that satisfies Rayleigh's necessary condition for barotropic instability—namely, the change in sign of the meridional gradient of absolute vorticity. In axisymmetric models, or in domains sufficiently narrow so as to prohibit large-scale zonal asymmetries, this unstable vorticity anomaly cannot undulate and roll up into vortices in the process of ITCZ breakdown (e.g., Nieto Ferreira and Schubert 1997). Such a process can occur in models with sufficiently wide domains; given that the most unstable wavelength in the barotropic instability problem is about 10 times the half-width of the vorticity anomaly (Kuo 1973; Joly and Thorpe 1990), we expect a domain width of 960 km to be just wide enough to accommodate the most unstable mode corresponding to an ITCZ that is 1° of latitude in meridional extent. This is only a rough estimate because the zonal-mean ITCZ typically has a meridional extent of several degrees latitude in the wide-domain model (e.g., Figs. 8d and 9), but this is a characteristic of the mean state with eddy activity, not of a basic state without eddies. The issue is also complicated by the fact that the circulation in this model has a strong baroclinic component and is strongly coupled to the diabatic effects of moist convection. Nevertheless, it

is clear that our domain is likely wide enough to permit the eddies involved in ITCZ breakdown but may also be narrow enough to influence or confine those vortices. We plan to explore the behavior in even wider domains in future work. We also note that the low-level absolute vorticity is anticyclonic between the equator and the convecting region (Fig. 9). Such inertially unstable vorticity distributions are hypothesized to be important in the 3–8-day time scales of east Pacific ITCZ variability (Toma and Webster 2010), but it is unclear whether there is any relevance to the longer time scales examined here.

Barotropic vortices on a beta plane migrate poleward by nonlinear advection in a process known as beta drift (Li and Wang 1994), and such poleward motion of vortices does succeed ITCZ breakdown in dry barotropic simulations (Nieto Ferreira and Schubert 1997). The beta drift of baroclinic vortices can be considerably more complicated because of interactions between upper- and lower-level vorticity anomalies (Wang and Holland 1996a). The baroclinic behavior is even less understood when such vortices are coupled to diabatic heat sources such as moist convection (Wang and Holland 1996b; Chan 2005). Such convectively coupled baroclinic behavior is relevant to the anomalies seen in this model, which exhibit closed cyclonic structures for at least part of their poleward trajectory, as seen in a sample event (Fig. 10). In this representative event, the vorticity field consists of numerous individual weak maxima when the precipitation is centered between 5° and 10°N and consists of a closed circular cyclone only between 10° and 18°N . By the time the vorticity and precipitation maxima reach 20°N , the vorticity anomaly has stretched into a zonally elongated strip that has some undulations and irregularities. This vortex strip propagates poleward to 30°N . The mechanisms responsible for this behavior are discussed in greater detail in the next section.

5. Mechanisms of propagation and instability

This section presents additional results and discussion regarding the mechanisms of instability and propagation of convective anomalies in the wide-domain model.

a. Propagation: Convectively coupled beta drift

Here we suggest that the frictional convergence produced by a poleward-drifting boundary layer cyclone generates low-level ascent that, in turn, produces deep convection. The generation of deep convection by Ekman convergence in a boundary layer cyclone was also hypothesized to be part of the mechanism of the poleward propagating ISO by Jiang et al. (2004) and Bellon and Sobel (2008b); the main difference here is that we argue that the low-level cyclone drifts poleward through the

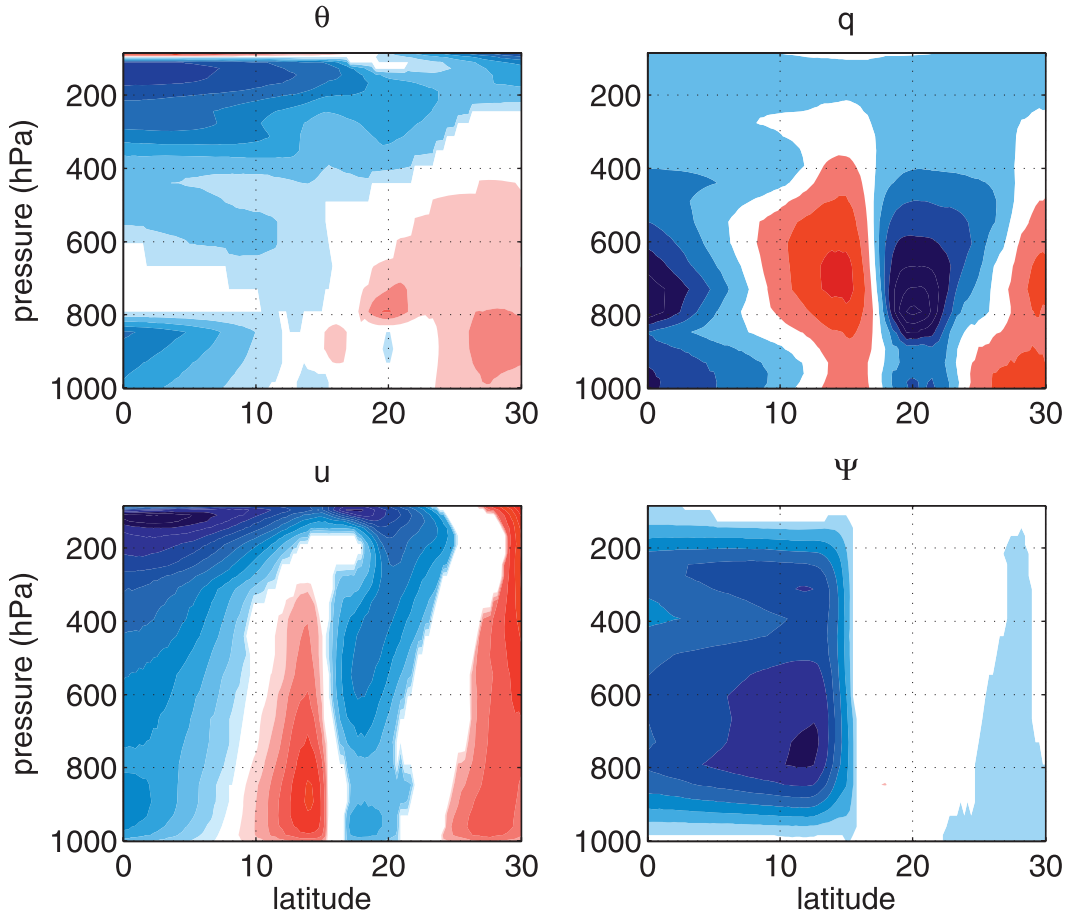


FIG. 8. Composite zonal-mean structure for the wide-domain model at 30-km horizontal resolution with RAVE factor 15, with composite based on precipitation at 15°N. Total rather than anomalous fields are shown, with a horizontal mean subtracted for the top panels as described in the text. (a) Potential temperature with a contour interval of 0.75 K, (b) specific humidity with a contour interval of 1 g kg⁻¹, (c) zonal wind with a contour interval of 2.5 m s⁻¹, and (d) mass streamfunction with a contour interval of 1×10^9 kg s⁻¹. Red (blue) shading denotes positive (negative) anomalies.

nonlinear and zonally asymmetric process of beta drift rather than through linear and zonally symmetric momentum advection in a baroclinic mean state. The details of how Ekman convergence generates deep convection merit further exploration, as Jiang et al. (2004) assumed convection is proportional to moisture convergence, which can be expected to generate CISK-like instability, whereas Bellon and Sobel (2008a) assumed a quasi-equilibrium closure that produces enhanced convection by a positive feedback with lower free-tropospheric moisture. Some form of the latter sort of moisture–convection feedback has been shown to operate in SAM (e.g., Kuang 2008, 2010) and has been discussed in the context of the eastward propagating MJO (e.g., Grabowski and Moncrieff 2004). Further exploration of the detailed mechanism by which Ekman convergence produces deep convection, in the context of the poleward propagating ISO, is left for future work; below we focus on the beta drift of low-level vortices.

1) DRY MODEL SIMULATIONS

Our hypothesized mechanism for propagation involves the poleward drift of low-level cyclones and the forcing of convection by those cyclones. To examine the first of these processes in isolation, we impose a steady deep heating anomaly in dry versions of the wide- and narrow-domain models and examine the time evolution of boundary layer vorticity. The heating anomaly Q is prescribed as a zonally symmetric step function in latitude and a quadratic function in pressure:

$$Q = Q_0 - \gamma \left(\frac{p - p_0}{p_s - p_0} \right)^2. \quad (3)$$

With a surface pressure $p_s = 1000$ hPa, we chose $p_0 = 600$ hPa and specified Q_0 and γ to be 4.8 and 4.0 K day⁻¹, respectively, between 9.5° and 10.5°N, and zero elsewhere.

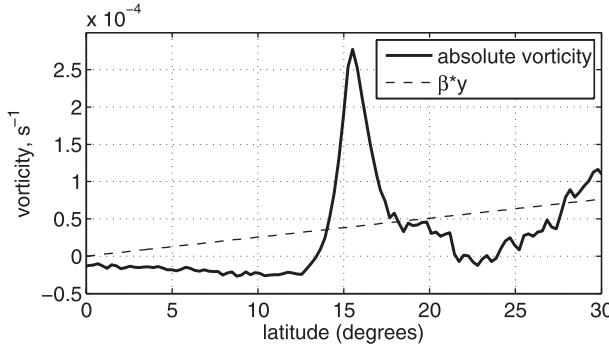


FIG. 9. Composite 900-hPa absolute vorticity (solid) and its planetary component (dashed) for the wide-domain model at 30-km horizontal resolution with RAVE factor 15.

This particular vertical structure, with a midtropospheric maximum, was chosen for consistency with Wang and Magnusdottir (2005), who conducted idealized simulations of the breakdown of a baroclinic vortex strip. This steady heating is imposed in the model with 30-km horizontal resolution and a RAVE factor of 15 with two different domain widths, 4 grid points (i.e., 120 km), and 32 grid points (i.e., 960 km). The integration is started from a state of rest with a meridionally uniform stable stratification. Surface friction is eliminated for simplicity, which allows for examination of the formation and drift of low-level vorticity anomalies without the added complication of Ekman convergence and adiabatic cooling by any associated ascent. No compensating heat sink is applied, so the model is not expected to reach a steady

state; this is not expected to be problematic since the unbalanced heating is applied in less than 1% of the domain and the model is integrated for only 40 days.

In the narrow domain, a zonal-mean surface vorticity maximum forms near the center of the heating and, over tens of days, migrates poleward by about 0.75° latitude to nearly the northward edge of the heating zone (Fig. 11a). The reason for this slight, slow poleward migration in the narrow-domain case is not obvious, since there is no pre-existing baroclinic flow and inspection of the wind fields shows no significant zonal asymmetries in the four-gridpoint-wide domain. One possibility is that meridional gradients in the mean state increase with time, as the planetary vorticity gradient causes meridional gradients of winds and isentropes to be stronger on the poleward side of the imposed heating. Indeed, inspection of the temperature field shows a weak Hadley-like circulation being set up, bounded by the heating region at its poleward edge. This circulation relaxes meridional temperature gradients south of the heating but allows a southward temperature gradient to grow at the poleward edge of the heating. In the stably stratified model with no surface temperature gradient poleward of the heating, this temperature distribution corresponds to the near-surface static stability being weaker on the poleward edge of the heating than on its equatorward edge, which necessitates a larger ascent on the poleward edge to balance the applied heating. This larger vertical motion produces a larger vorticity tendency, shifting the vorticity maximum toward the poleward edge of the heating. The total

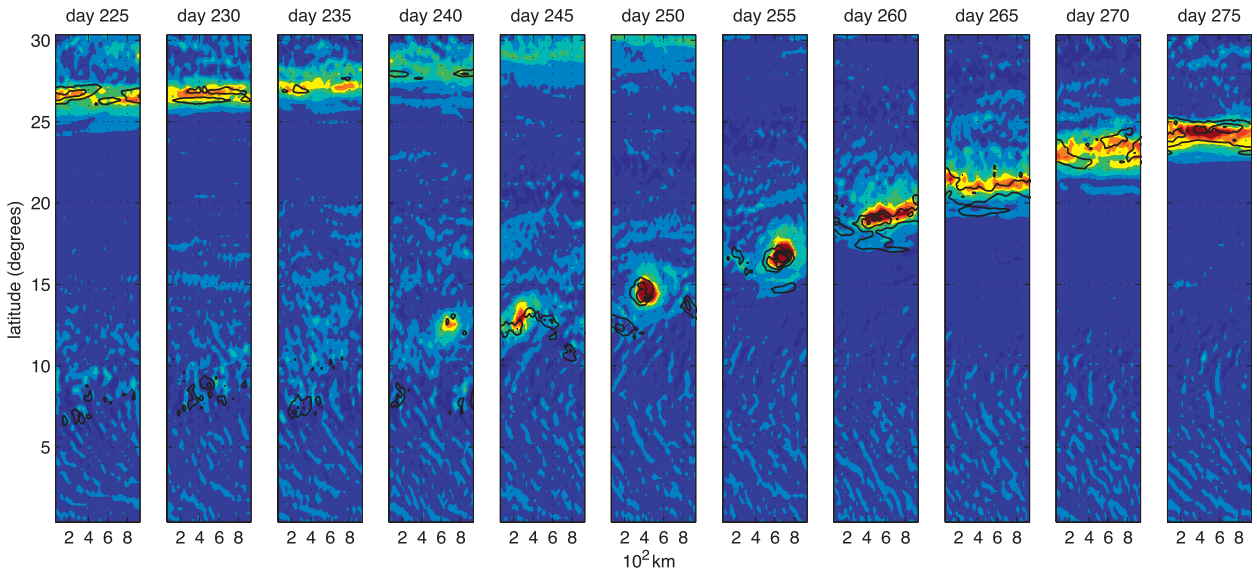


FIG. 10. Daily-mean relative vorticity at 900 hPa (color shading) and precipitation rate (contours) for a series of days from the wide-domain model at 30-km horizontal resolution with RAVE factor 15. Contour interval is $1 \times 10^{-4} \text{ s}^{-1}$ for vorticity and 80 mm day^{-1} for precipitation.

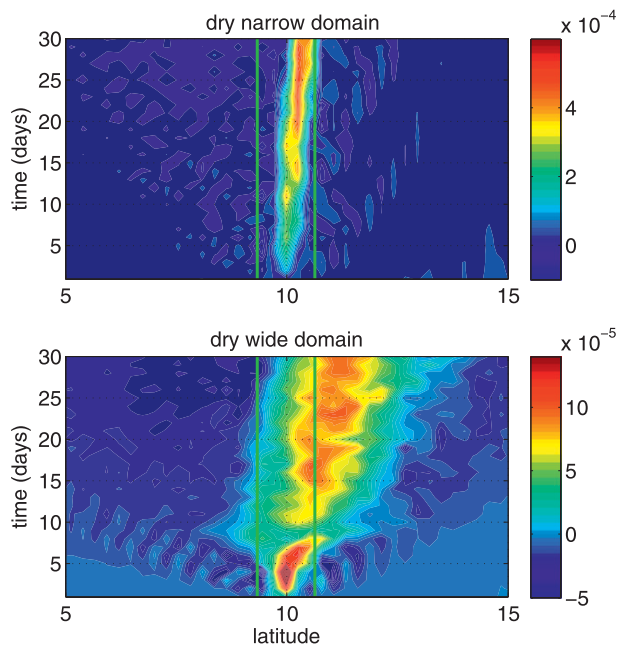


FIG. 11. Time series of zonal-mean surface relative vorticity for the dry model with (top) a narrow domain that is four grid points wide at 30-km horizontal resolution and (bottom) the standard wide domain at 30-km horizontal resolution, both employing a RAVE factor of 15. The thermal forcing was applied between the vertical green lines; contour interval is (top) $2 \times 10^{-5} \text{ s}^{-1}$ and (bottom) $0.5 \times 10^{-5} \text{ s}^{-1}$.

poleward drift is small, though, with the vorticity maximum not even leaving the heating region after 30 days.

Surface vorticity in the wide-domain model exhibits high-amplitude zonal asymmetries, and its maximum drifts poleward until it is clearly separated from the heating region (Fig. 11b). Plan views of the surface vorticity are consistent with the process of ITCZ breakdown and subsequent beta drift of the resulting vorticity anomalies (Fig. 12). A nearly zonally symmetric vorticity maximum formed during the first few days of integration, and then this vortex strip began to undergo ITCZ breakdown, separating into three vorticity maxima (day 4) that then broke apart and drifted outside the bounds of the heating (days 6 and 8). By day 20 the individual vorticity maxima had merged and formed a single larger vortex centered about 1° of latitude poleward of the heating region. This entire process is similar in many respects to that shown by Nieto Ferreira and Schubert (1997) for barotropic flow and by Wang and Magnusdottir (2005) for baroclinic flow, in which a zonally elongated heating produces an ITCZ that undulates and breaks down into vortices, which then propagate poleward by the process of beta drift. The propagation speed is much slower in the dry model than in the moist model, possibly because the moist model cyclone is coupled with moist convection.

Although in this dry model the process of ITCZ breakdown forms the vortices that later migrate poleward through the process of beta drift, it is unclear whether ITCZ breakdown itself plays an important role in the moist wide-domain model. Prior to the initiation of a poleward propagating event, the precipitation and vorticity fields consist of a group of seemingly unorganized, pointlike maxima between 5° and 10°N (Fig. 10). A closed vorticity maximum emerges from this unorganized field, which suggests that the process of convective self-aggregation (e.g., Bretherton et al. 2005) may be more relevant than the process of ITCZ breakdown to event initiation in this model. The fact that the initiation of a poleward propagating event was greatly delayed by eliminating the effect of moisture on the rates of radiative cooling, as is shown below, is consistent with this self-aggregation hypothesis. ITCZ breakdown may be more relevant at latitudes poleward of about 18°N , where the vorticity maximum has become zonally elongated into a vortex strip (this is discussed in more detail below).

2) DIAGNOSIS OF BETA GYRES

In the process of beta drift, a vortex in a background state with a nonzero meridional gradient of absolute vorticity perturbs its environment by advecting the background vorticity meridionally on the east and west sides of the initial vortex. This advection creates vorticity anomalies, or beta gyres, east and west of the vortex, and those anomalies in turn produce flow that advects the initial vortex. We examine whether beta gyres exist in a composite event from the wide-domain model, using a diagnostic similar to that employed in studies of tropical cyclone motion (Fiorino and Elsberry 1989). In this diagnostic we take the horizontal streamfunction of the nondivergent flow at 900 hPa and retain only the radially asymmetric part of that streamfunction relative to the vortex center, which is defined as the local streamfunction minimum. Using a frame of reference where the vortex center is the origin, this radially asymmetric streamfunction is averaged over all events, with an event defined when precipitation is maximum at 15°N , as in our previous composites. This composite asymmetric streamfunction is then used to compute the radially asymmetric, nondivergent wind. A beta drift vector is obtained by averaging that wind over the central part of the composite vortex having relative vorticity larger than $1 \times 10^{-4} \text{ s}^{-1}$. Because the relationship between this beta drift vector and the total vortex motion is sensitive to the area over which the radially asymmetric flow is averaged (Wang and Li 1992), and because a quantitative assessment of vortex motion speed would require analysis of all terms in the vorticity budget, we use the

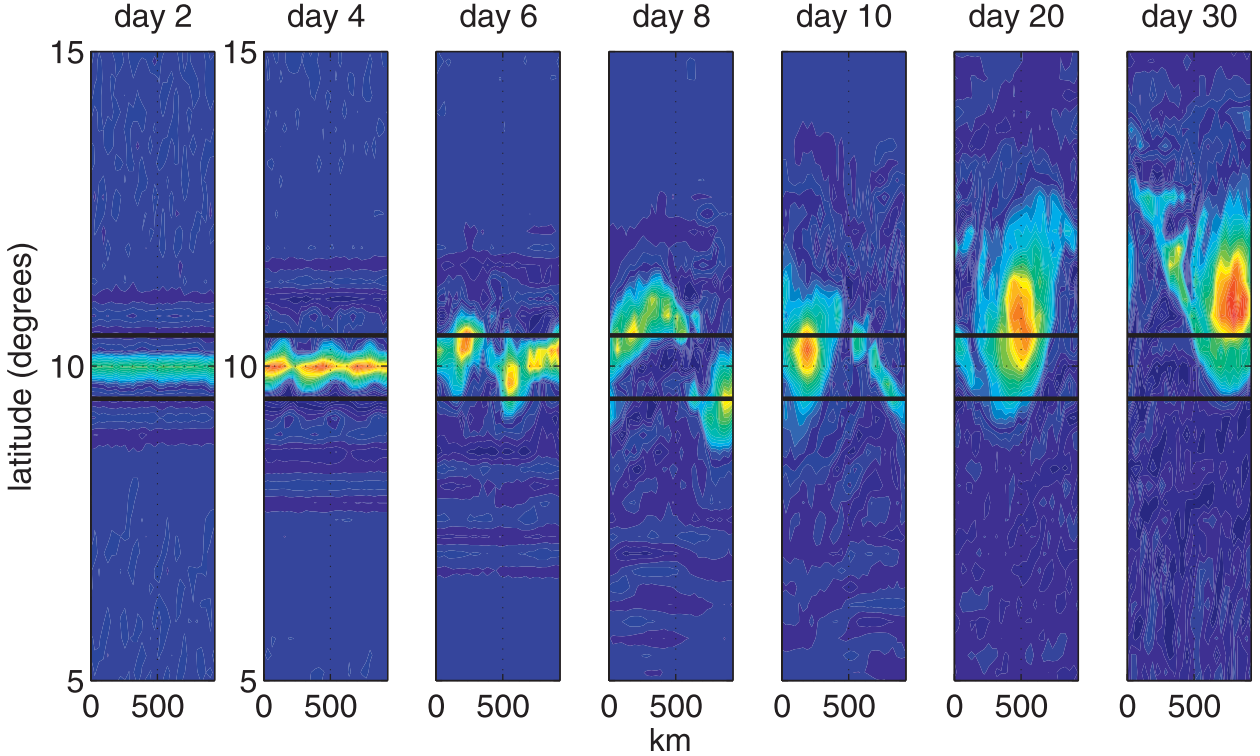


FIG. 12. Daily-mean surface relative vorticity on a series of days for the wide-domain dry model. The thermal forcing was applied between the horizontal black lines, and the contour interval is $1 \times 10^{-5} \text{ s}^{-1}$.

beta drift vector only as an indicator of the direction of beta drift (i.e., its magnitude is not compared with the propagation speed).

This diagnostic shows that the composite vortex has a northeast–southwest tilt, consistent with advection by the initial vortex creating a cyclonic anomaly west of that vortex and an anticyclonic anomaly to the east (Fig. 13). The radially asymmetric streamfunction shows flow across the vortex from the southwest toward the north and northeast; the mean flow across the vortex, as indicated by the beta drift vector, is toward the northeast. Beta drift is commonly thought to produce flow-relative vortex motion to the northwest, but this is true only for an isolated, barotropic vortex with no diabatic or frictional sources of potential vorticity (PV). Beta drift can be more complicated for baroclinic vortices that are coupled to moist convection (e.g., Chan 2005), and Wu and Emanuel (1993) found that a baroclinic vortex in background shear indeed moved northward to northeastward. Although this diagnostic does not assess the magnitude of nonlinear advection relative to all other terms in the vorticity budget, it shows that the zonally asymmetric vorticity in a composite event from the wide-domain model produces vortex advection in the correct direction to explain the propagation.

In the wide-domain moist model, the vortices become zonally elongated near and poleward of 20°N and their poleward propagation slows. We suggest that the elongation occurs because of horizontal shear, which is indeed strongest between about 20° and 27°N in this model (these latitudes constitute the poleward boundary of the time-mean cross-equatorial Hadley cell, where strong off-equatorial westerlies decrease quickly with latitude; not shown). A vortex strip that is closed in the zonal direction and is exactly zonally symmetric would not drift poleward by the process of beta drift. However, the zonally elongated vortex strip that exists in our wide-domain model near and north of 20°N is not strictly zonally symmetric. It does contain some zonal asymmetries, and although these asymmetries are clearly weaker than those seen at lower latitudes in the model, the weaker nature of these asymmetries would be consistent with the slower propagation that occurs once the vortex becomes zonally elongated. It is possible that zonally symmetric vorticity advection, as described by Jiang et al. (2004) or Bellon and Sobel (2008b), may also play a role, although it is unclear why this same process would not have occurred in the narrow-domain model. Further work with simpler theoretical models is needed to understand these dynamics.

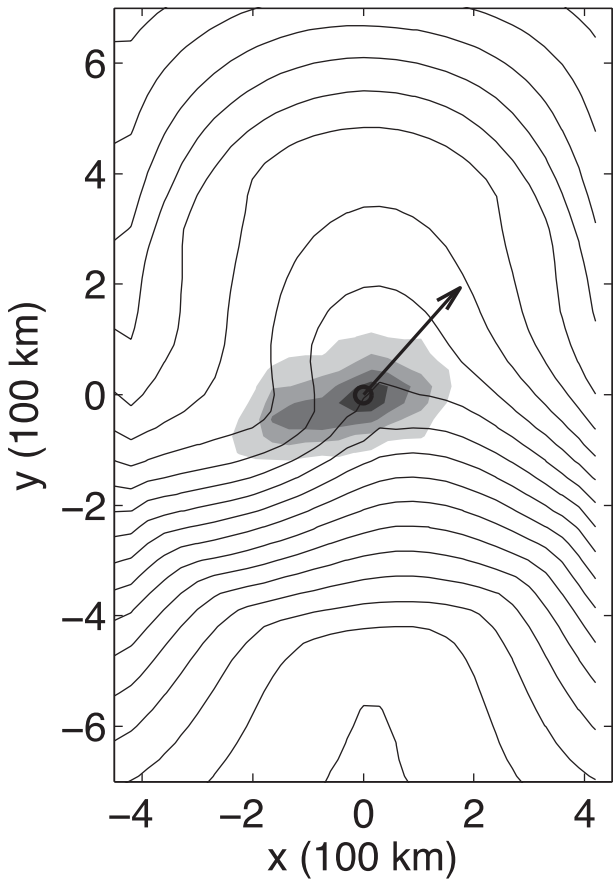


FIG. 13. Composite relative vorticity (shading) and radially asymmetric component of the nondivergent streamfunction, both at 900 hPa, for the moist wide-domain model. The composite is based on precipitation at 15°N, and averages across events were taken in a coordinate system using the vortex center as origin. The vector indicates the radially asymmetric nondivergent horizontal wind averaged over the central region of the vortex.

b. Instability: A moist static energy budget view

Now we turn to the moist static energy budget of the wide-domain model to better understand the instability mechanisms responsible for maintaining the anomalies against dissipation.

The model used here represents changes between the solid, liquid, and vapor phases of water, and so conserves frozen moist static energy (FMSE), which differs from the standard moist static energy by the addition of an ice term:

$$h_f = c_p T + gz + Lq_v - L_f q_{ice}. \quad (4)$$

Henceforth any use of the term “moist static energy” refers to this definition of FMSE.

We examine the vertically integrated budget of FMSE in the wide-domain model:

$$\frac{\partial \langle h_f \rangle}{\partial t} + \langle \mathbf{v} \cdot \nabla h_f \rangle = \mathbf{E} + \langle \mathbf{R} \rangle, \quad (5)$$

where angle brackets denote a mass-weighted vertical integral from the surface to the top of the atmosphere, and both \mathbf{v} and the gradient operator are three-dimensional. The net surface enthalpy flux is denoted by \mathbf{E} , the radiative cooling by \mathbf{R} , and the three-dimensional vector wind by \mathbf{v} . The vertically integrated horizontal diffusion was found to be small compared to all other terms in the budget for the cases examined here, and so was neglected in the above conservation equation. Composites were formed by averaging over events defined based on precipitation at 15°N, as was done for the composites of vertical structure presented in section 4, and anomalies were computed by subtracting time means after the first 100 days of integration.

The composite anomalous moist static energy budget from the wide-domain, 30-km-resolution model shows a positive $\langle h_f \rangle$ anomaly centered near 13°N (Fig. 14). This $\langle h_f \rangle$ anomaly results almost entirely from the humidity anomaly in the lower free troposphere (seen in Fig. 8b). The time tendency of $\langle h_f \rangle$ is positive north of this anomaly and negative south of it, consistent with its northward migration. This total tendency is due almost entirely to advection. The net advective tendency results from a balance between horizontal and vertical components, each of which has a larger amplitude than the net tendency at most latitudes (Fig. 14c). Further decomposition of the advective tendencies into components due to zonal-mean flow and eddies shows that zonally asymmetric eddies account for a large part of the advective tendencies. Although it is difficult to infer the mechanism of propagation from such tendencies alone, the structure of the horizontal advective tendency is also consistent with the hypothesis that the moist static energy anomaly propagates poleward by self-advection, analogous to a mechanism proposed for eastward propagation of the MJO (Benedict and Randall 2007; Sugiyama 2009; Maloney et al. 2010). Assessing the degree to which propagation by this sort of self-advection is compatible with the beta drift hypothesis proposed in the previous section requires more detailed examination of the gross moist stability and the structure of the eddies, a task left for future work.

The source terms \mathbf{R} and \mathbf{E} have a large component that is in phase with the $\langle h_f \rangle$ anomaly, which suggests that they might contribute to the instability of the anomalies. The \mathbf{E} anomaly peaks south of the positive $\langle h_f \rangle$ anomaly because the cyclonic westerlies that lie south of this anomaly exist in a region of time-mean monsoonal westerlies. The advective tendency is thus partially opposed by the \mathbf{E} tendency, so that \mathbf{E} anomalies would also

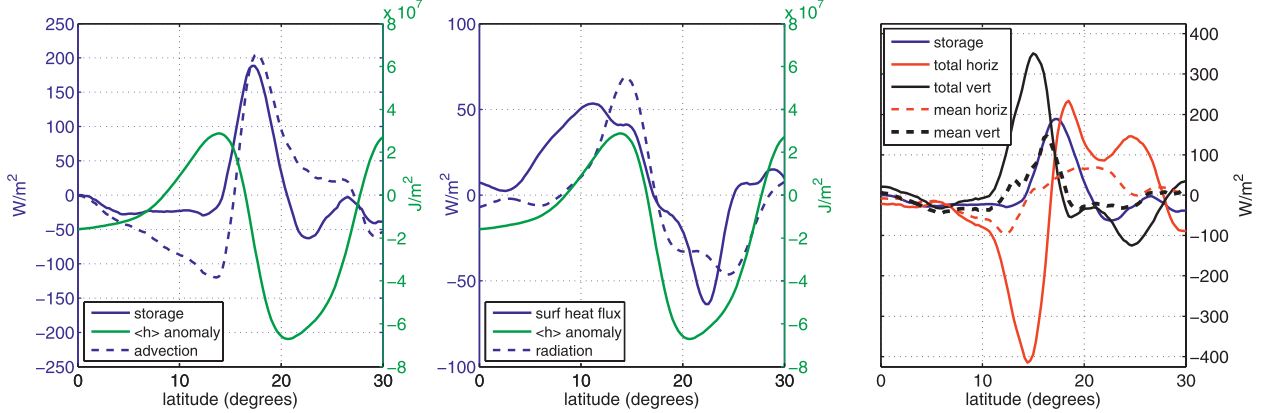


FIG. 14. Terms in the vertically integrated frozen moist static energy budget for a composite anomaly in the wide-domain model at 30-km horizontal resolution with RAVE factor 15. The green line in the left two panels shows the vertically integrated moist static energy anomaly. (left) Time tendency of moist static energy (solid blue) and the tendency due to advection (dashed blue). (middle) Tendencies due to surface enthalpy fluxes (solid blue) and radiation (dashed blue). (right) Total time tendency (solid blue), the tendencies due to horizontal and vertical advection (solid red and black lines, respectively), and the advective tendencies computed using zonal-mean quantities (dashed lines).

seem to slow the speed of poleward propagation. These ideas were tested by conducting an integration of the wide-domain model at 30-km resolution (and RAVE factor 15) with surface sensible and latent heat fluxes set to their latitude-dependent, zonal- and time-mean values from the control run. Another integration was conducted with fully interactive surface heat fluxes, but with interactive radiation replaced by a latitude- and height-dependent temperature tendency equal to the zonal- and time-mean net radiative cooling from the control run. We henceforth refer to these as “perturbed physics” integrations, both of which were conducted using the standard SST distribution [i.e., $\Delta T = 20$ K in (1)].

In the integration with prescribed surface heat fluxes, regular poleward propagation still occurred, but with a higher frequency and propagation speed than in the control run (Fig. 15; cf. Fig. 7). This increased propagation speed is consistent with the idea that wind-evaporation feedback slows the poleward propagation of the anomalies, as discussed above and by Bellon and Sobel (2008b), and similar to the role played by WISHE in some theories for the eastward propagating MJO (e.g., Maloney and Sobel 2004). In this run with prescribed surface heat fluxes, however, the poleward propagating anomalies decreased strongly both in amplitude and in the meridional distance they transit after the first 100 days. This might be due to a drift in the mean state away from that produced in the control run, and it is interesting to note that this attenuation of the events did not occur when surface heat fluxes were fixed in an integration employing the weaker SST gradient corresponding to $\Delta T = 10$ K (using the time-mean surface flux distribution from a control run with that same,

weaker SST gradient; result not shown). Nevertheless, we produced composites for the run with fixed surface heat fluxes and $\Delta T = 20$ K based on only the first two poleward propagating events. These composites show that without interactive surface heat fluxes, both the positive \mathbf{R} anomaly and the positive $\langle h_f \rangle$ anomaly have

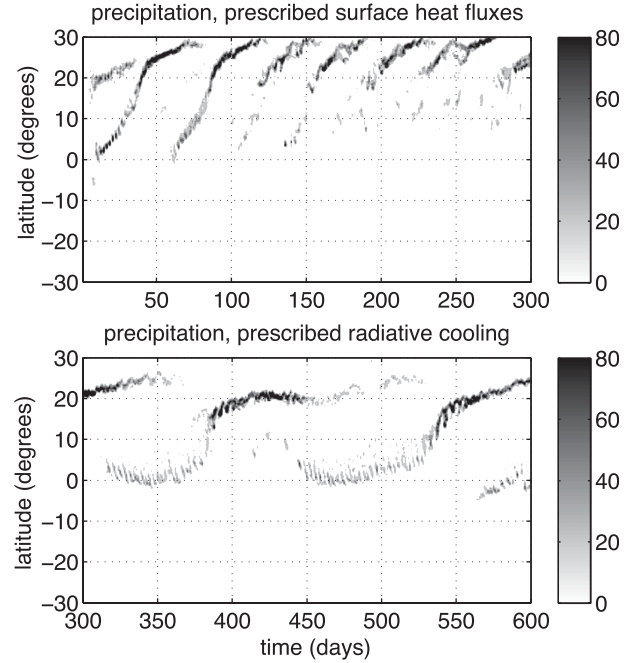


FIG. 15. Time series of precipitation (mm day^{-1}) for perturbed physics integrations of the wide-domain model at 30-km horizontal resolution with RAVE factor 15, for the runs with (top) time-invariant surface enthalpy fluxes and (bottom) time-invariant radiative cooling.

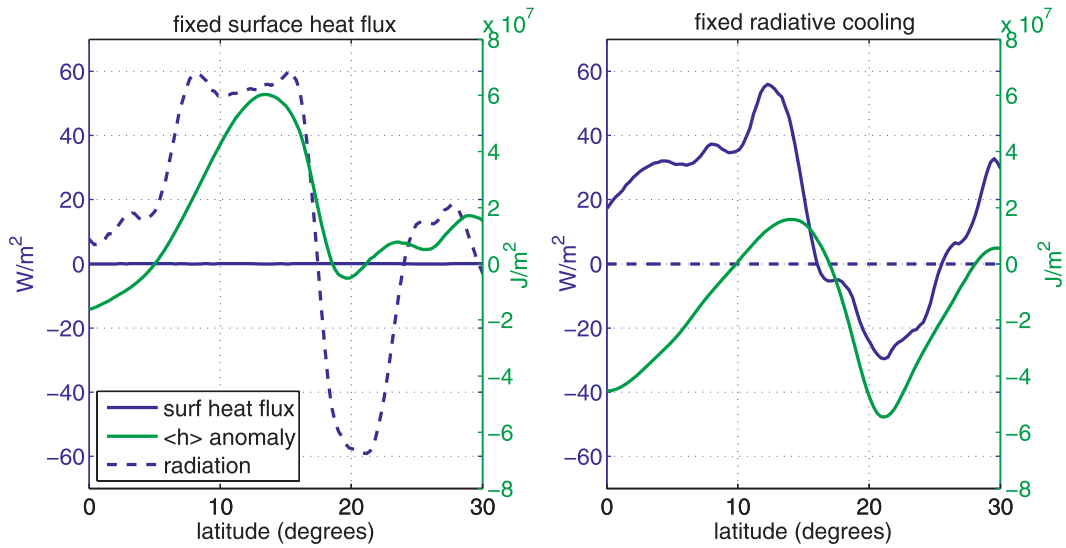


FIG. 16. Terms in the vertically integrated moist static energy budget for a composite anomaly in the wide-domain model at 30-km horizontal resolution with RAVE factor 15. Both panels show the moist static energy anomaly (green lines, right y axis), the time tendency due to surface enthalpy fluxes (solid blue, left y axis), and the tendency due to radiation (dashed blue, left y axis). Runs shown are (left) with time-invariant surface enthalpy fluxes and (right) with time-invariant radiative cooling.

a larger meridional extent than in the control run (cf. Figs. 14b and 16a). Also, the zonal wind became much more strongly baroclinic, with an increased southward tilt with height and surface westerlies nearly collocated with peak precipitation (cf. Figs. 8c and 17a).

The character of the anomalies also changed dramatically when radiative cooling was prescribed. The anomalies had similar propagation speeds but occurred less frequently than in the control run: the ITCZ typically persisted several degrees north of the equator for over

70 days before beginning its poleward migration (Fig. 15b). This is consistent with the idea mentioned in the previous section that a moisture–radiation feedback enhances the speed of convective self-aggregation and cyclogenesis. The meridional structure of the surface heat flux anomaly is qualitatively similar to that in the control case, consisting of a broad positive signal stretching from the equator to about 15°N (cf. Figs. 14b and 16b). The zonal wind anomalies also changed, having no discernable southward tilt with height in this run with prescribed

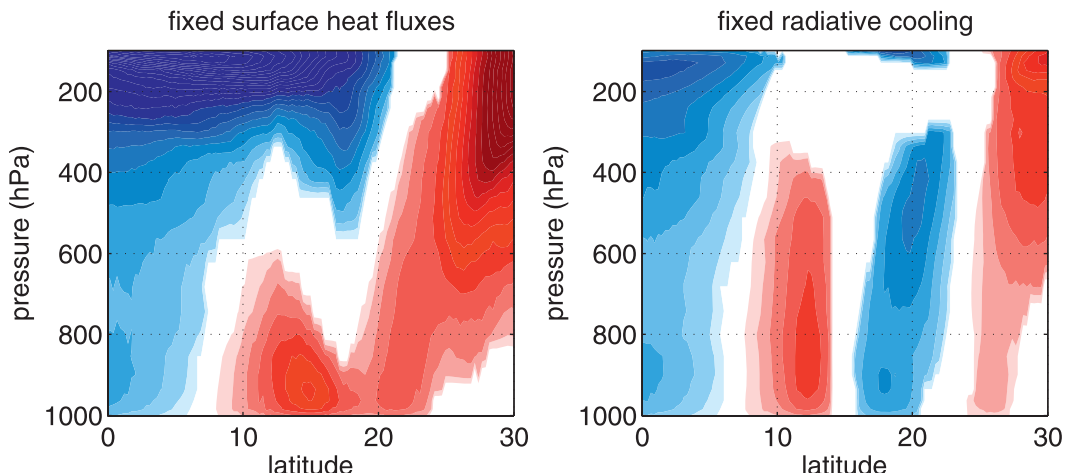


FIG. 17. Composite zonal wind for the wide-domain model with (left) prescribed surface enthalpy fluxes and (right) prescribed radiative cooling, with events selected based on precipitation at 15°N. Contour interval is 2.5 m s^{-1} . Red (blue) shading denotes positive (negative) anomalies.

radiative cooling (Fig. 17). When both surface heat fluxes and radiative cooling were prescribed, no poleward propagating events occurred and the model equilibrated in a state with two steady precipitation maxima near 3° and 22°N (not shown).

Together, these perturbed physics integrations and moist static energy budget diagnostics suggest that both wind–evaporation feedback and moisture–radiation feedback contribute to the instability of the poleward propagating anomalies. Enhanced surface heat fluxes on the equatorward side of the $\langle h_f \rangle$ anomaly seem to slow the poleward propagation speed. Interactive radiative cooling reduces the time the ITCZ spends just north of the equator before commencing its poleward migration. In the absence of only one of these feedbacks, repeated poleward propagation persists, but with altered phase speed, frequency, and dynamical structure. The reasons for the difference in dynamical structure between the run with fixed surface heat fluxes and the run with fixed radiative cooling are intriguing but are not explored further here.

6. Summary and conclusions

Multiple theories for the dynamics of the poleward propagating ISO have been formulated based on results from axisymmetric models using parameterized convection, but none of these theories has been tested in a model with explicit convection. For this reason, we examined the time-dependent circulation in a CSRM on a beta plane extending from 70°N to 70°S. Two versions of the CSRM were employed: one with a narrow zonal dimension of 4–16 km and another with a wider dimension of 960 km. The narrow domain was effectively axisymmetric on the large scale, with any eddy activity occurring at and below the mesoscale. Even the wider of these two domains still had a zonal extent that was small compared to its meridional extent and so could not represent the Rossby gyres associated with the MJO. It could, however, represent higher-wavenumber ITCZ eddies (e.g., Wang and Magnusdottir 2005) that were assumed by previous studies to simply act diffusively on the moisture field (e.g., Sobel and Neelin 2006). It is worth noting that previous authors who posited that poleward propagation occurred because of the modification of Rossby waves by easterly vertical shear (Wang and Xie 1997) have since shown that the role played by easterly shear can be represented in axisymmetric frameworks (Drbohlav and Wang 2007; Jiang et al. 2004). In other words, the fact that none of our models is wide enough to represent Rossby gyres may be incidental, since that mechanism can be represented in an axisymmetric framework.

Results from the narrow-domain CSRM differed greatly from results from previous studies that obtained deep, robust, poleward propagating convective anomalies in axisymmetric models using parameterized convection (e.g., Webster and Chou 1980; Jiang et al. 2004; Bellon and Sobel 2008a). In some cases, convective anomalies did propagate meridionally in the narrow-domain CSRM, but these anomalies had a spatial structure that was shallow and inconsistent with that of the observed poleward propagating ISO. Propagating anomalies in the narrow-domain model were also highly sensitive to SST and vanished for higher resolutions. While these anomalies may be valid solutions of some configurations of the CSRM, we consider them to have little relevance to the observed poleward propagating ISO.

The reasons for the difference between results from our narrow-domain CSRM and those from axisymmetric models using parameterized convection are not obvious and merit further exploration. It is possible that axisymmetric models used in previous studies have some deficiency in their parameterizations of subgrid-scale physics, such as moist convection or radiation, or in their representation of large-scale dynamics.

Deep, robust, poleward propagating anomalies were produced in the CSRM with the wider zonal dimension of 960 km. These anomalies exhibited meridional phase relationships between convection and zonal wind similar to those seen in observations and were fairly insensitive to changes in horizontal resolution and SST. Diagnostics from this model suggest a new mechanism for poleward propagation of the ISO: the beta drift of low-level cyclones produces Ekman pumping poleward of existing convection, and this Ekman pumping produces enhanced free-tropospheric humidity that shifts the convection poleward. Strong low-level cyclones seemed to self-organize 5°–10° north of the equator in our moist wide-domain model, with convective aggregation possibly enhanced by a moisture–radiation feedback. Convective anomalies seem to originate closer to the equator in observations (e.g., Goswami 2005), perhaps because zonally propagating disturbances such as Kelvin waves and the MJO produce organized convective vortices that can move poleward through beta drift.

Multiple instability mechanisms seem to operate in the wide-domain CSRM, as poleward propagating events were produced when interactive surface enthalpy fluxes or radiation were turned off individually but not simultaneously. However, the structure of the anomalies changed significantly in the absence of either of these feedbacks. Diagnostics of the moist static energy budget, together with an integration using prescribed surface enthalpy fluxes, suggest that wind–evaporation feedback strongly slows the poleward propagation of the anomalies, thereby

playing an important role in setting the period of the anomalies. These findings suggest that idealized models that omit either interactive radiation or interactive surface heat fluxes may be missing physics that shape the dynamical structure of a phenomenon, even though such models obtain unstable modes that propagate in the correct direction.

The mechanisms suggested in this study do require further testing in models with realistic boundary conditions and also in simpler theoretical models. Furthermore, observations should be examined to determine if the zonally elongated bands of convection in the boreal summer ISO are comprised of smaller-scale vorticity anomalies having structures consistent with their poleward propagation by beta drift. Despite this need for further work, these results provide a new candidate mechanism for the poleward propagation of the boreal summer ISO and illustrate the complexity and non-unique nature of instability in CSRsMs.

Acknowledgments. Matthew Peters wrote the software to calculate the vertically integrated moist static energy budget. Computations were run on the Odyssey cluster supported by Harvard University's FAS Research Computing Group. WRB was supported by the Reginald A. Daly Postdoctoral Fellowship in the Department of Earth and Planetary Sciences at Harvard, and by the John and Elaine French Environmental Fellowship at the Harvard University Center for the Environment. ZK was supported by NSF Grant ATM-0754332.

REFERENCES

- Annamalai, H., and J. M. Slingo, 2001: Active/break cycles: Diagnosis of the intraseasonal variability of the Asian summer monsoon. *Climate Dyn.*, **18**, 85–102.
- Arakawa, A., 2004: The cumulus parameterization problem: Past, present, and future. *J. Climate*, **17**, 2493–2525.
- Bellon, G., and A. H. Sobel, 2008a: Poleward-propagating intraseasonal monsoon disturbances in an intermediate-complexity axisymmetric model. *J. Atmos. Sci.*, **65**, 470–489.
- , and —, 2008b: Instability of the axisymmetric monsoon flow and intraseasonal oscillation. *J. Geophys. Res.*, **113**, D07108, doi:10.1029/2007JD009291.
- Benedict, J., and D. Randall, 2007: Observed characteristics of the MJO relative to maximum rainfall. *J. Atmos. Sci.*, **64**, 2332–2354.
- Bretherton, C., P. Blossey, and M. Khairoutdinov, 2005: An energy-balance analysis of deep convective self-aggregation above uniform SST. *J. Atmos. Sci.*, **62**, 4273–4292.
- Chan, J., 2005: The physics of tropical cyclone motion. *Annu. Rev. Fluid Mech.*, **37**, 99–128.
- Drbohlav, H.-K. L., and B. Wang, 2005: Mechanisms of the northward-propagating intraseasonal oscillation: Insights from a zonally symmetric model. *J. Climate*, **18**, 952–972.
- , and —, 2007: Horizontal and vertical structures of the northward-propagating intraseasonal oscillation in the South Asian monsoon region simulated by an intermediate model. *J. Climate*, **20**, 4278–4286.
- Fiorino, M., and R. Elsberry, 1989: Some aspects of vortex structure related to tropical cyclone motion. *J. Atmos. Sci.*, **46**, 975–990.
- Fu, X., B. Wang, and L. Tao, 2006: Satellite data reveal the 3-D moisture structure of tropical intraseasonal oscillation and its coupling with underlying ocean. *Geophys. Res. Lett.*, **33**, L03705, doi:10.1029/2005GL025074.
- Goswami, B. N., 2005: South Asian summer monsoon. *Intraseasonal Variability in the Atmosphere–Ocean Climate System*, W. Lau and D. Waliser, Eds., Praxis, 125–173.
- Grabowski, W. W., and M. W. Moncrieff, 2004: Moisture–convection feedback in the tropics. *Quart. J. Roy. Meteor. Soc.*, **130**, 3081–3104.
- Jiang, X., and D. Waliser, 2008: Northward propagation of the subseasonal variability over the eastern Pacific warm pool. *Geophys. Res. Lett.*, **35**, L09814, doi:10.1029/2008GL033723.
- , T. Li, and B. Wang, 2004: Structures and mechanisms of the northward propagating boreal summer intraseasonal oscillation. *J. Climate*, **17**, 1022–1039.
- Joly, A., and A. Thorpe, 1990: Frontal instability generated by tropospheric potential vorticity anomalies. *Quart. J. Roy. Meteor. Soc.*, **116**, 525–560.
- Jones, C., L. Carvalho, R. W. Higgins, D. Waliser, and J. Schemm, 2004: Climatology of tropical intraseasonal convective anomalies: 1979–2002. *J. Climate*, **17**, 523–539.
- Kemball-Cook, S., and B. Wang, 2001: Equatorial waves and air-sea interaction in the boreal summer intraseasonal oscillation. *J. Climate*, **14**, 2923–2942.
- Khairoutdinov, M., and D. Randall, 2003: Cloud-resolving modeling of the ARM summer 1997 IOP: Model formulation, results, uncertainties, and sensitivities. *J. Atmos. Sci.*, **60**, 607–625.
- Kiehl, J., J. Hack, G. Bonan, B. Boville, D. Williamson, and P. Rasch, 1998: The National Center for Atmospheric Research Community Climate Model: CCM3. *J. Climate*, **11**, 1131–1149.
- Krishnamurti, T. N., and H. N. Bhalme, 1976: Oscillations of a monsoon system. Part I: Observational aspects. *J. Atmos. Sci.*, **33**, 1937–1954.
- Kuang, Z., 2008: Modeling the interaction between cumulus convection and linear gravity waves using a limited-domain cloud system-resolving model. *J. Atmos. Sci.*, **65**, 576–591.
- , 2010: Linear response functions of a cumulus ensemble to temperature and moisture perturbations and implication to the dynamics of convectively coupled waves. *J. Atmos. Sci.*, **67**, 941–962.
- , P. N. Blossey, and C. S. Bretherton, 2005: A new approach for 3D cloud-resolving simulations of large-scale atmospheric circulation. *Geophys. Res. Lett.*, **32**, L02809, doi:10.1029/2004GL021024.
- Kuo, H., 1973: Dynamics of quasigeostrophic flows and instability theory. *Adv. Appl. Mech.*, **13**, 247–330.
- Lawrence, D. M., and P. J. Webster, 2001: Interannual variations of the intraseasonal oscillation in the South Asian summer monsoon region. *J. Climate*, **14**, 2910–2922.
- , and —, 2002: The boreal summer intraseasonal oscillation: Relationship between northward and eastward movement of convection. *J. Atmos. Sci.*, **59**, 1593–1606.
- Li, X., and B. Wang, 1994: Barotropic dynamics of the beta gyres and beta drift. *J. Atmos. Sci.*, **51**, 746–756.
- Lin, J., K. Weickman, G. Kiladis, B. Mapes, S. Schubert, M. Suarez, J. Bacmeister, and M. Lee, 2008: Subseasonal variability associated with Asian summer monsoon simulated by 14 IPCC AR4 coupled GCMs. *J. Climate*, **21**, 4541–4567.

- Lindzen, R. S., and S. Nigam, 1987: On the role of sea surface temperature gradients in forcing low-level winds and convergence in the tropics. *J. Atmos. Sci.*, **44**, 2418–2436.
- , and A. Y. Hou, 1988: Hadley circulations for zonally averaged heating centered off the equator. *J. Atmos. Sci.*, **45**, 2416–2427.
- Madden, R. A., and P. R. Julian, 1972: Description of global-scale circulation cells in the tropics with a 40–50-day period. *J. Atmos. Sci.*, **29**, 1109–1123.
- Maloney, E., and A. Sobel, 2004: Surface fluxes and ocean coupling in the tropical intraseasonal oscillation. *J. Climate*, **17**, 4368–4386.
- , D. Chelton, and S. Esbensen, 2008: Subseasonal SST variability in the tropical eastern North Pacific during boreal summer. *J. Climate*, **21**, 4149–4167.
- , A. Sobel, and W. M. Hannah, 2010: Intraseasonal variability in an aquaplanet general circulation model. *J. Adv. Model. Earth Syst.*, **2**, 5, doi:10.3894/JAMES.2010.2.5.
- Nieto Ferreira, R., and W. Schubert, 1997: Barotropic aspects of ITCZ breakdown. *J. Atmos. Sci.*, **54**, 261–285.
- Nolan, D., C. Zhang, and S. Chen, 2007: Dynamics of the shallow meridional circulation around intertropical convergence zones. *J. Atmos. Sci.*, **64**, 2262–2285.
- Palmer, T., 1994: Chaos and predictability in forecasting the monsoons. *Proc. Indian Natl. Sci. Acad.*, **60**, 57–66.
- Pauluis, O., D. Frierson, S. Garner, I. Held, and G. Vallis, 2006: The hypohydrostatic rescaling and its impacts on modeling of atmospheric convection. *Theor. Comput. Fluid Dyn.*, **20**, 485–499.
- Sikka, D. R., and S. Gadgil, 1980: On the maximum cloud zone and the ITCZ over Indian longitudes during the southwest monsoon. *Mon. Wea. Rev.*, **108**, 1840–1853.
- Sobel, A., 2007: Simple models of ensemble-averaged tropical precipitation and surface wind, given the sea surface temperature. *The General Circulation of the Atmosphere*, T. Schneider and A. H. Sobel, Eds., Princeton University Press, 219–251.
- , and J. Neelin, 2006: The boundary layer contribution to intertropical convergence zones in the quasi-equilibrium tropical circulation model framework. *Theor. Comput. Fluid Dyn.*, **20**, 323–350.
- , E. D. Maloney, G. Bellon, and D. M. Frierson, 2008: The role of surface heat fluxes in tropical intraseasonal oscillations. *Nat. Geosci.*, **1**, 653–657, doi:10.1038/ngeo312.
- Srinivasan, J., S. Gadgil, and P. Webster, 1993: Meridional propagation of large-scale monsoon convective zones. *Meteor. Atmos. Phys.*, **52**, 15–35.
- Sugiyama, M., 2009: The moisture mode in the quasi-equilibrium tropical circulation model. Part II: Nonlinear behavior on an equatorial β plane. *J. Atmos. Sci.*, **66**, 1525–1542.
- Toma, V., and P. Webster, 2010: Oscillations of the intertropical convergence zone and the genesis of easterly waves. Part I: Diagnostics and theory. *Climate Dyn.*, **34**, 587–604.
- Wang, B., and H. Rui, 1990: Synoptic climatology of transient tropical intraseasonal convective anomalies. *Meteor. Atmos. Phys.*, **44**, 43–61.
- , and X. Li, 1992: The beta drift of three-dimensional vortices: A numerical study. *Mon. Wea. Rev.*, **120**, 579–593.
- , and X. Xie, 1997: A model for the boreal summer intraseasonal oscillation. *J. Atmos. Sci.*, **54**, 72–86.
- Wang, C., and G. Magnusdottir, 2005: ITCZ breakdown in three-dimensional flows. *J. Atmos. Sci.*, **62**, 1497–1512.
- Wang, Y., and G. Holland, 1996a: The beta drift of baroclinic vortices. Part I: Adiabatic vortices. *J. Atmos. Sci.*, **53**, 411–427.
- , and —, 1996b: The beta drift of baroclinic vortices. Part II: Diabatic vortices. *J. Atmos. Sci.*, **53**, 3737–3756.
- Webster, P. J., 1983: Mechanisms of monsoon low-frequency variability: Surface hydrological effects. *J. Atmos. Sci.*, **40**, 2110–2124.
- , 2006: The coupled monsoon system. *The Asian Monsoon*, B. Wang, Ed., Springer, 3–66.
- , and L. C. Chou, 1980: Low-frequency transitions of a simple monsoon system. *J. Atmos. Sci.*, **37**, 368–382.
- Wheeler, M., and H. Hendon, 2004: An all-season real-time multivariate MJO index: Development of an index for monitoring and prediction. *Mon. Wea. Rev.*, **132**, 1917–1932.
- Wu, C.-C., and K. Emanuel, 1993: Interaction of a baroclinic vortex with background shear: Application to hurricane movement. *J. Atmos. Sci.*, **50**, 62–76.
- Yasunari, T., 1979: Cloudiness fluctuation associated with the Northern Hemisphere summer monsoon. *J. Meteor. Soc. Japan*, **57**, 227–242.